



# Numerical modeling of extreme wave interaction with point-absorber using OpenFOAM

Eirini Katsidoniotaki <sup>\*</sup>, Malin Göteman

*Department of Electrical Engineering, Uppsala University, Lägerhyddsvägen 1, SE-752 37, Uppsala, Sweden*

## ARTICLE INFO

### Keywords:

Extreme waves  
100-year return period  
Wave energy converter  
Point-absorber  
Overset mesh  
OpenFOAMv1906

## ABSTRACT

Extreme waves are critical for the WEC's development. CFD toolboxes have been widely used in the simulation of extreme waves-structure interaction. However, the quality of the mesh is a sensitive issue; the WEC's large response can lead to mesh deformation and subsequent numerical instability. In this paper, 100-year extreme waves are chosen from the environmental contour of the Humboldt Bay site in California, and their interaction with the WEC is modeled using the open-source CFD software OpenFOAM. The overset mesh technique is an advanced method recently available in OpenFOAM, able to handle great body motions. Here, the overset method is utilized and compared with the commonly used morphing method. The two methods provide equivalent results, but the latter is prone to the mesh deformation and fails to complete the simulations. Regarding the impact of extreme waves on WECs, the results further show that the combination of wave height and steepness is critical; i.e., the 100-year wave height does not necessarily result in the maximum forces, but rather steeper sea states tend to contribute in higher wave loadings. Additionally, the WEC is studied for 40% higher generator's damping, as it is a common control strategy during the harsh environmental conditions.

## 1. Introduction

Wave energy is considered part of the future energy mix ([World Bank, 2017](#); [European Commission, 2020](#)), but only a few WEC concepts have been operated in a sea environment. According to the Joint Research Centre Ocean Energy Database ([Magagna et al., 2016](#)), the technology readiness level for wave energy converters (WECs) ranges between 5 to 8, which means that their commercial viability is yet to be proven. A big challenge is to guarantee the survivability in the offshore extreme conditions, since the extreme loads is a key cost driver for the wave energy technology ([Jenne et al., 2015](#); [Neary et al., 2014](#)). That is to say, underestimation of loads may lead to component failures and high repair costs, whereas overestimation could result in increased structural costs and possibly reduced performance during moderate wave conditions.

Considerable experience, knowledge, industrial guidelines and standards are available on traditional offshore systems, such as shipping, oil & gas, and increasingly for offshore wind. However, the standards need to be tailored for the wave energy sector since there are large uncertainties related to the prediction of wave loads on WECs. The devices are small and often with dynamical behavior, designed to be in resonance with the waves, therefore, the established knowledge from the traditional offshore industry cannot be readily translated on the WECs. Currently, there are a few technical specifications ([International](#)

[Electrotechnical Commission, 2019, 2015; DNV, 2010; Norsok Standard, 2007](#)) providing the best practices for WEC design, yet systematic standardization is required particularly for extreme conditions. Several studies, both numerical and experimental, have confirmed that it is not always the largest wave that causes the largest load ([Chaplin and Rainey, 2012; Coe et al., 2014; Göteman et al., 2015; Yu et al., 2015](#)). Instead, the largest load depends on the combinations of different wave parameters, such as wave height and period, and also on the history of device's motion ([Katsidoniotaki et al., 2020](#)). The problem is further complicated by the fact that wave energy has not converged around one or a few concepts, but comprises a multitude of fundamentally different technologies. As a result, the extreme wave impact on WECs, the survivability and failure risk mitigation, are issues that need to be addressed.

In offshore engineering, structures are typically designed to withstand loads corresponding to waves with a certain site-specific exceedance probability, such as waves with 100-years return period. These rare and large waves are difficult and costly to be reproduced in experimental wave tanks, therefore, the contribution of numerical tools is fundamental. Potential flow methods are the standard approach to model wave-structure interaction in presence of small-amplitude waves, yet extreme waves are high and steep involving nonlinear

\* Corresponding author.

E-mail addresses: [eirini.katsidoniotaki@angstrom.uu.se](mailto:eirini.katsidoniotaki@angstrom.uu.se) (E. Katsidoniotaki), [malin.goteman@angstrom.uu.se](mailto:malin.goteman@angstrom.uu.se) (M. Göteman).

dynamics and large amplitude structural response. To capture such effects, high-fidelity computational fluid dynamics (CFD) methods are recommended (Giorgi and Ringwood, 2017; Folley, 2016). With the use of high-performing computer clusters, previously infeasible CFD tools are becoming increasingly accessible (Kim et al., 2016), and the usage of a numerical wave tank (NWT) to model the wave–structure interaction has received increasing attention in recent years (Katsidoniaki et al., 2021; Windt et al., 2020b, 2018b; Van Rij et al., 2018; Palm et al., 2016; Ransley et al., 2017a; Sjökvist et al., 2017; Wolgamot and Fitzgerald, 2015).

The widely used high-fidelity CFD approach is based on the Reynolds-averaged Navier–Stokes equations over a discretized mesh, using the volume of fluid method to capture the free surface (Ransley et al., 2017b). Due to the high and steep waves the structural response is expected to be large and the computational mesh has to adapt to large deformations. The morphing dynamic mesh is considered the most commonly used method, due to its simplicity and general applicability (Windt et al., 2018b), but often leads to reduced mesh quality and fatality of simulations. More advanced methods, such as re-meshing (Chen et al., 2017) and overset (Windt et al., 2020a; Katsidoniaki and Göteman, 2020) could be utilized in order to overcome this issue. In the present study, the overset dynamic mesh method is selected, in which the numerical wave tank consists of at least two different overlapping mesh regions, each one maintaining the mesh structure and quality during the simulation. For commercial CFD softwares, like STAR-CCM+, the overset method was already available, but for the open-source CFD software OpenFOAM has been implemented from the version 1706 and later. It is very important to assess the capabilities of a toolbox widely available to the research community to perform advanced simulations, such as the extreme wave–structure interaction. However, a limited number of WEC simulations has been carried out using the new overset mesh function of OpenFOAM (Windt et al., 2020a; Katsidoniaki and Göteman, 2020; Windt et al., 2019a; Chen et al., 2019b,a; Windt et al., 2018a).

This work has been highly motivated by Windt et al. (2020a,b). The purpose of this study is twofold: one objective is evaluate the capability of the open-source CFD software OpenFOAM to simulate the extreme wave–structure interaction utilizing the overset dynamic mesh method. The popular morphing dynamic mesh method is also implemented and the two methods are compared for 100-year return period waves. The second point of this work is to study the extreme wave impact on a point-absorber WEC connected to a direct-driven linear generator with limited stroke length. The role of the generator's damping is of high relevance for extreme wave conditions. In Göteman et al. (2015), a similar WEC was studied experimentally for three different dampings in extreme waves, and it was seen that the PTO damping affected the obtained peak forces to a large degree. This has served as a motivation for the choice of the PTO dampings studied in this paper. Five sea states along the 100-year return contour for the Humboldt Bay site in California have been chosen, and are modeled as equivalent regular waves. The dynamics of the WEC and the force on critical components are analyzed, and the impact of the limited stroke length and the damping of the generator are evaluated.

The structure of the paper is as follows. In Section 2 the methods for the extreme sea state selection, the WEC concept utilized in this study, and the numerical model settings are presented. The results are presented and discussed in Section 3, and conclusions of the study are drawn in Section 4.

## 2. Methods

### 2.1. Extreme sea states selection and realization

The evaluation of the WEC's dynamics in extreme waves and the identification of extreme design loads is a critical stage of the design process. Statistical methods are implemented for the identification of

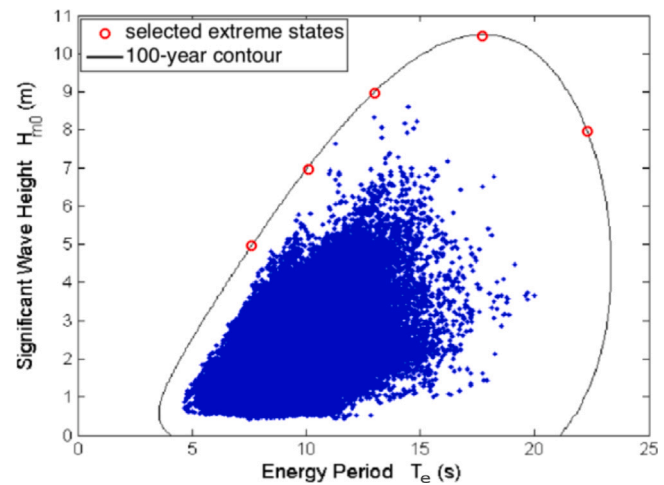


**Fig. 1.** The selected extreme sea states are marked with red circles on the 100-year contour of the Humboldt bay site, in California.

Source: Figure adopted from Quon et al. (2016).

the  $n$ -year extreme sea states at an offshore site, where  $n = 50, 100$ , etc. In particular, the environmental contour is a popular bivariate approach considering the joint distribution of wave height and period for the  $n$ -year waves characterization (DNV, 2010; Wrang et al., 2021).

Also there is a discussion about the most realistic way to represent numerically a stochastic sea state. In Coe et al. (2018), three alternatives are mentioned as the way to realize a sea state. The most direct way is by 3-hours irregular wave time series, yet this approach is computationally expensive for high-fidelity numerical models, even with access to high-performing computer clusters. Another approach is the representation of the sea state as an equivalent regular wave train. In this case, assuming that the wave elevation follows a Rayleigh distribution, the maximum individual wave occurs during a sea state has wave height equal to:  $H_{max} = 1.9H_s$ , with  $H_s$  being the significant wave height (Ochi, 2005). Therefore,  $H_{max}$  is considered as the wave height of the equivalent regular wave and period  $T = T_p$  (Yu et al., 2015). According to the third approach, a sea state can be represented as a focused wave, and several methodologies for the generation of the focused wave profile are suggested, such as NewWave theory, most-likely-extreme response, etc.

In the present work, five sea states with 100-year return period along the environmental contour of the selected site are used. Fig. 1 shows the environmental contour which has been generated based on measurements from the Coastal Data Information Program #128 station and the National Data Buoy Center #46212 buoy near Humboldt Bay, California (Quon et al., 2016). Each sea state is realized as an equivalent regular wave with wave characteristics as listed in Table 1.

### 2.2. Wave energy converter

The WEC considered in this paper is based on the wave energy device developed at Uppsala University, Sweden. The concept has been realized in several full-scale WECs that have been tested offshore at the Lysekil test site (Leijon et al., 2008). It consists of a floating cylindrical buoy connected to a direct-driven linear generator placed at the seabed. The values of the WEC's dimensions and characteristics are given in Table 2 while the schematic view of the generator is illustrated in Fig. 2. The generator comprises a translator moving vertically within a stator, and the changing magnetic field induces electricity in the stator windings. The translator is pulled upwards by the buoy motion and downwards by its own weight, and is restricted to move within a limited stroke length. End-stop springs are mounted at the upper and lower position of the PTO in order to dampen the forces on the

**Table 1**

Wave characteristics of the selected five sea states and their equivalent regular wave profile. The period,  $T$ , of the equivalent wave is taken equal to the peak period,  $T_p$ , of the sea state. The Keulegan-Carpenter,  $KC$ , and Reynolds,  $Re$ , numbers are also provided (Section 2.4.1).

Sea state	Sea states characteristics			Equivalent regular wave				
	$H_s$	$T_e$	$T_p$	$H_{max}$	$T$	Steepness[%]	$KC$	$Re \times 10^6$
1	5	7.6	8.2	9.5	8.2	9.1	9	12.5
2	7	10.1	11.7	13.3	11.7	6.5	12	12
3	9	13	15.1	17.1	15.1	5.4	16	12
4	10.5	17.7	20.5	19.95	20.5	4.2	18.5	10.4
5	8	22.3	25.9	15.2	25.9	2.4	14	6.3

generator hull when the translator hits the upper and lower end-stops. In particular once the translator hits the upper or lower end-stop spring an additional restraint force is added  $F_{spring}$ , which is calculated as:

$$F_{spring} = \begin{cases} -k_s z_t(t), & \text{if } |z_t| > L_{free} \\ 0 & \text{otherwise} \end{cases} \quad (1)$$

where  $L_{free}$  is the free stroke length,  $k_s$  is the spring constant and  $z_t$  the position of the translator described by a single vertical coordinate. When the translator exceeds the total stroke length, i.e. when the upper end-stop spring is fully compressed as depicted in Fig. 2c, two scenarios are expected: (i) Once the translator is on the upper maximum position, apart from the  $F_{spring}$ , an additional force is triggered. The connection line starts to act as an elastic mooring line adding a further restraint force,  $F_{add}$  given by Eq. (2), where  $k_{ML}$  and  $\delta l$  are the stiffness and the elongation of the connection line,

$$F_{add} = -k_{ML} \delta l \quad (2)$$

(ii) The buoy and the translator are coupled by the connection line as long as it is stiff, but once the translator rests on the lower end-stop position the connection line is slack and  $F_{Line} = 0$ . In that case the motion of the translator and the buoy is considered uncoupled.

The translator motion, and thus the buoy motion, is damped by the applied generator damping force,  $F_d$ :

$$F_d = -\gamma \dot{z}_t(t) \quad (3)$$

where  $\gamma$  the damping coefficient. In both experiments and numerical simulations, it has been seen that peak loads during extreme wave events can be reduced by an increased generator damping which prevents the translator to hit the end-stops (Göteman et al., 2015; Sjökvist et al., 2017). For this reason, two different generator dampings are studied in this paper. The restraint acting on the buoy due to linear PTO system is added through the connection line force  $F_{line}$ , with direction along a fixed point on the buoy to a fixed point on the seabed. The total forces acting on the buoy is the sum of hydrodynamic forces, the line force and the gravitational force, as described by Eq. (4).

Eq. (5) describes the line force,  $F_{line}$ , which expresses the forces acting on the PTO.

$$m_b \ddot{r} = \iint p \hat{n} dS - F_{line} - m_b g \quad (4)$$

$$F_{line} = -m_t g + F_d + F_{spring} + F_{add} \quad (5)$$

where  $m_b$  is the mass of the buoy,  $r$  denotes the position of the buoy,  $p$  is the pressure on the buoy surface,  $\hat{n}$  is the unit vector normal to the buoy surface,  $g$  is the acceleration of gravity,  $m_t$  is the mass of the translator. In this point, it is worth mentioning that the position  $r$  of the buoy in six DoF is related to the position of the translator  $z_t$  by the equations of motions for the two systems (Eqs. (4) and (5)), which are related through the line force,  $F_{line}$ .

In the OpenFOAM simulations, the above described restraint is applied by an in-house developed code coupling with sixDoFRigidBodyMotion library. The Uppsala University WEC utilizing this restraint has been previously validated against experimental tests as can be found in Sjökvist et al. (2017), Engström et al. (2017) and Sjökvist and Göteman (2016, 2019).

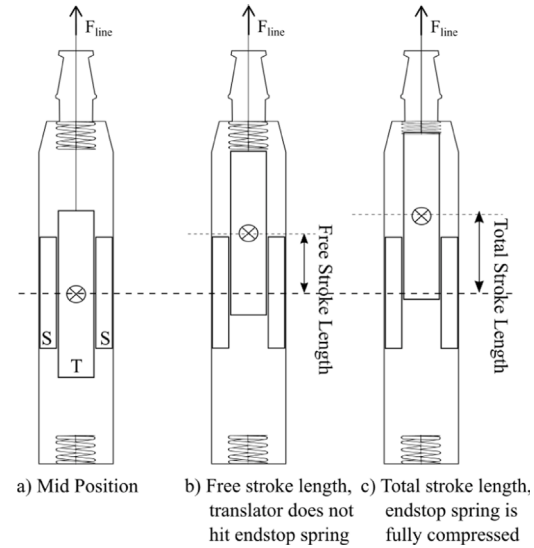


Fig. 2. An illustration of the direct-driven linear generator with limited stroke length.  
Source: Figure adopted from Sjökvist and Göteman (2019).

**Table 2**  
Dimensions and characteristic values of the point-absorber WEC.

Parameter	Value
Buoy radius	1.7 m
Buoy height	2.12 m
Buoy draft	1.3 m
Buoy mass	5736 kg
Translator mass	6240 kg
Generator damping 1	59 kN
Generator damping 2	83 kN
Upper end-stop spring coefficient	776 kN/m
Upper end-stop spring length	0.6 m
Max stroke length upper/lower	1.8/1.8 m
Spring constant of connection line	300 kN/m

### 2.3. Dynamic mesh methods

In CFD solvers, dynamic mesh motion is required to change over the time due to a prescribed motion or the dependency in the flow motion. The physical problem of fluid–structure interaction leads to flow-induced boundary deformations. The present paper focuses on dynamic mesh methods (DMMs) for motion, in which the number and connectivity of mesh elements remain unchanged (no topological changes).

The computational grid is supposed to follow the changing shape of the boundary, guaranteeing mesh quality without user interaction. The mesh motion equations are resolved automatically in order to define the mesh deformation. The design of the OpenFOAM software, based on object-oriented programming, provides an advantage in the coupling of its dynamic mesh features with the physics solvers (Jasak and Tuković, 2010). In OpenFOAM, the sixDoFRigidBodyMotion library solves

both the translational and rotational motion of the body, based on the forces that the body experiences due to the interaction with the fluid motion and external forces. This library is applied during the solution when a DMM is implemented in order to provide information about body motion and the mesh is then adapted to the new body position.

### 1. Morphing mesh

The finite volume method is adapted to the moving polyhedral mesh and the mesh motion is obtained by solving the mesh motion equation, defined by the Laplace equation  $\nabla \cdot (k \nabla u) = 0$ , where  $u$  describes the velocity of the moving boundary and  $k$  the diffusivity. The diffusivity parameter,  $k$ , is a measure for mesh deformation and quality (Davidson et al., 2019), and controls how the motion of a moving boundary (WEC) is diffused into the domain, finding an efficient way to distribute the mesh motion. In OpenFOAM, the morphing mesh area is defined by specifying the `innerDistance` and `outerDistance` parameters. The mesh motion solver applies spherical linear interpolation (SLERP) to define the mesh displacement based on the distance of each cells from the moving body (Shoemake, 1985).

### 2. Overset mesh

In recent versions of OpenFOAM, version 1706 and later, the overset mesh functionality has been launched as an alternative to the existing morphing mesh method. Overset mesh has the capability to represent complex geometries under various wave conditions, preserving a good mesh quality. The overset mesh technique allows the overlapping of several mesh components, where each component mainly captures a certain part of the domain. Once the mesh components are defined, they are assembled and flow information is exchanged between the overlapping mesh components (Chen et al., 2019a; Guerrero, 2006). Every time step, the following steps are performed:

- *Identification of hole cells:* The cells inside or close to the objects are identified and deactivated, since these cells (the so-called hole cells) are not included in the calculations. In the present study, the region where the buoy is normally located (yellow region in Fig. 3) is the hole cells region. For moving objects, the identification of hole cells is repeated every time step which is a time consuming process.
- *Identification of acceptor cells:* Close to hole cells, the acceptor cells are adjusted and could be identified as both background and body-fitted. Through the acceptor cells, flow information is exchanged between different mesh components. Governing equations are not discretized at these cells, rather information passes through interpolation. However, their presence is essential for finite volume discretization for the cells adjacent to them. In the present study `inverseDistance` interpolation method is used (Lemaire et al., 2019).
- *Identification of donor cells and information exchange:* For each acceptor cell, several cells from a neighbor mesh component are identified as donor cells. These cells are used in creating the interpolation equations for flow variables at acceptor's cell centers. The green region in Fig. 3 represents the interpolation region where acceptor and donor cells interact each other.

### 2.4. Numerical modeling

The fluid motion is described by the Navier–Stokes equations, but the numerical solvers in order to average out part of the turbulence unsteadiness in the Navier–Stokes equations implement the Reynolds-averaged Navier–Stokes (RANS) approach. One of the most widely used turbulence models in ocean engineering applications is the SST  $k - \omega$  model (see Windt et al., 2020a), and this is the turbulence model used

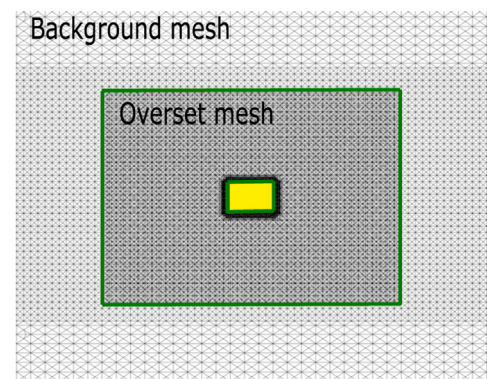


**Fig. 3.** Schematic of the quadratic mesh employed with triangulation of the cells. The overset mesh (body-fitted mesh) follows the motion of the WEC. The background mesh covers the greater part of the NWT. Schematic of the quadratic mesh employed with triangulation of the cells.

**Table 3**

Evaluation of NWT length considering four lengths;  $2.5\lambda, 3.5\lambda, 4.5\lambda, 5.5\lambda$ . RMSE [%] value calculation for the surface elevation measured at the buoy position, having as reference the case of  $5.5\lambda$ .

Length	RMSE <sub>1</sub> [%]	RMSE <sub>4</sub> [%]
$2.5\lambda$	5.2	4.4
$3.5\lambda$	1.4	0.97
$4.5\lambda$	0.4	0.26

also in this paper. The RANS for two incompressible fluids, i.e. air and water, are solved using the cell-centered finite volume method. The free surface is approximated through the volume of fluid method as presented by Weller and McIntyre (2019). In the present analysis, the CFD software OpenFOAMv1906 was utilized. Due to the overset dynamic mesh method, the two phase solver `interFoam` is adapted to `overInterDyMFoam` solver and the so-called PIMPLE algorithm is used for pressure–velocity coupling. The motion of the floating body is solved by the standard `sixDoFRigidBody` library. Each simulation runs for  $14T$ , where  $T$  is the period of the regular wave, with a ramp time of  $2T$  and variable time step adjusted to the Courant–Friedrichs–Lowy (CFL) condition with maximum CFL number equal to 0.5.

#### 2.4.1. Numerical wave tank

The NWT follows a parametric dimensioning based on the wave length,  $\lambda$ , therefore it is adapted to each one of the examined sea states. The NWT spans a length of  $3.5\lambda$  in the wave propagation direction ( $x$ -direction) and  $1\lambda$  in the direction perpendicular to the wave propagation ( $y$ -direction). In the  $z$ -direction, the NWT spans  $2d$ , where  $d$  is the water depth and is equal to 70 m. The still water level is at  $z = 0$  and the floating body is placed  $1.3\lambda$  downwards the wave generation boundary, and  $2.2\lambda$  upwards from the absorption boundary (Fig. 4).

In order to choose the proper length for the NWT, a study considering four lengths was conducted;  $2.5\lambda, 3.5\lambda, 4.5\lambda, 5.5\lambda$ . In this study, the NWT was empty (without the WEC) and the length changes by modifying the distance of the outlet boundary from the location where the buoy will be placed later. Moreover, for the proper selection of the length two waves were evaluated; the sea state with the steepest wave (sea state 1) and the sea state with the highest wave (sea state 4). For each case, the surface elevation is measured at the position where the buoy will be placed, and compared with the reference case of  $5.5\lambda$ . The comparison is based on the root-mean-square-error (RMSE) and the values are listed in Table 3. The length of  $3.5\lambda$  was considered as the best option due to the small RMSE value and the reduced computational cost required for a shorter domain.

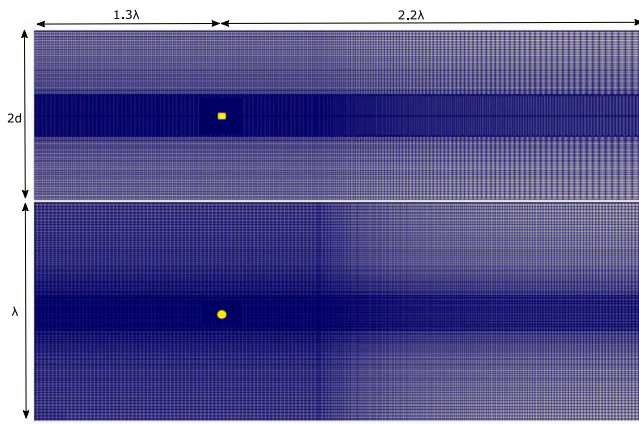


**Fig. 4.** The dimensions of the NWT are shown as a function of the wave length,  $\lambda$ , and the water depth,  $d$ . The upper and lower pictures depict the side ( $x$ - $z$  plane) and the top ( $x$ - $y$  plane) view.

The computational mesh consists of three regions: (i) the background mesh, (ii) a higher resolution region close to free water surface which is extended in total  $2H$  below and above the still water level, (iii) an even higher resolution region around the floating body. In region (ii) the spatial discretization is one level higher than the background mesh, i.e. 20 cells per wave height (CPH) utilizing square cells (aspect ratio, AR = 1) up to  $0.4\lambda$  downwards the WEC position. To reduce the computational cost, the cells are stretched gradually until AR = 4 for the rest of the NWT length. In the  $y$ -direction, square cells are utilized in the region within  $6R$ , where  $R$  is the radius of the buoy, but further than that the cell stretching is also applied gradually until AR = 3. In the  $z$ -direction, the background mesh, extended above and below the refinement free surface region, is stretched until AR = 2. The region (iii) included the floating body and spans  $6.5R$ ,  $3R$  and  $4.7R$  in the  $x$ ,  $y$ ,  $z$ -direction, respectively. For the overset mesh method, the region (iii) represents the overset region. Detailed description about the resolution study is provided in Section 2.5. The size of the computational mesh is approximately 3.5, 5.6, 7.3, 11.6, 16 million cells for sea states 1, 2, 3, 4 and 5 respectively.

Keulegan–Carpenter (KC) and Reynolds (Re) numbers are important non-dimensional parameters that can provide an understanding of the physics of the flow and the hydrodynamic quantities. In particular, the KC number describes the relative importance of drag forces compared to inertial forces and it is dependent on the amplitude of the oscillation ( $\alpha$ ) and a characteristic length which is taken equal to the diameter of the floating body,  $D$ ;  $KC = 2\pi\alpha/D$  (Keulegan and Carpenter, 1958). Offshore structures generally experience high Reynolds number flows ( $Re > 10^6$ ) (Ong, 2017). The definition of the Reynolds number is  $Re = U \cdot D/v$ , where  $U = \pi \cdot H/T$  describes the characteristic free stream velocity and  $v$  the kinematic viscosity of the water. KC and Re values for the examined sea states are listed in Table 1. Both numbers take large values, justifying the choice of turbulent modeling solution in the present application.

#### 2.4.2. Wave generation and absorption

IHFOAM is a newly developed toolbox based on OpenFOAM, specially designed for offshore engineering applications (Higuera et al., 2013). The specific boundary conditions applying the static boundary method allow the generation and absorption of any wave type in the 3D numerical wave tank, from the most simple regular waves to complex irregular multi-directional sea states. For wave generation, the selected wave theory determines the wave velocity and surface elevation at the inlet boundary, while for the wave absorption the incoming fluxes are canceled by applying at the outlet boundary an opposite uniform velocity profile based on shallow water equation.

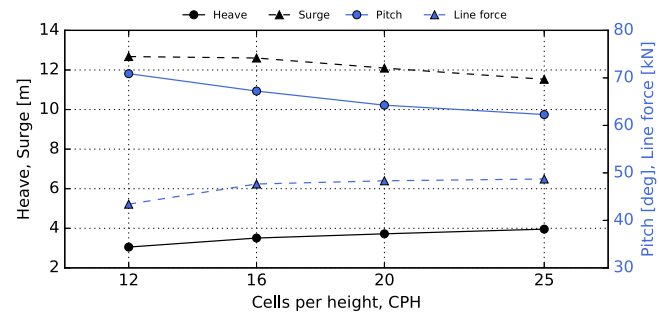


**Fig. 5.** Mesh convergence study for the sea state with highest steepness.

One of the favorable characteristics of IHFOAM is the reduced computational cost compared to other wave generation libraries (Windt et al., 2019b), thus it has been utilized in similar studies as the current one (Chen et al., 2019a,b; Windt et al., 2020a). In the present paper long waves are mainly examined, and according to Miquel et al. (2018), the long waves are better absorbed by the active wave absorption. The reduced computational cost and the satisfying absorption level of the long waves make the IHFOAM toolbox a proper choice for this study.

#### 2.4.3. Applied boundary conditions

The NWT consists of six walls, each being assigned with appropriate boundary conditions for each variable as listed in Table 4. The initial values of the turbulence model SST  $k - \omega$  are related to the celerity of the incoming wave, with  $k$  being the turbulence kinetic energy and  $\omega$  is the specific dissipation rate. In this study, wall functions are employed to approximate the turbulence in the near-wall region and the first cell centered is placed in the log-law region ensuring the accuracy of the result. The  $y+$  values of the simulations should be in the range of  $y+ \in [30, 200]$  (Davidson, 2015).

#### 2.5. Mesh convergence

The accuracy of the numerical solution in NWTs is also dependent on the degree of uncertainty due to spatial and temporal discretization levels. Methods of examining discretization errors are presented in Roache (1998). In the present work, verification of spatial discretization errors has been conducted considering the number of cells per wave height (CPH), focusing on the area close to the water surface. Worth noting here is that the discretization in the body-fitted mesh component is one level higher than the area close to the water surface, therefore, the mesh resolution around the body also changes during the convergence study. Four discretization levels have been examined; 12 CPH, 16 CPH, 20 CPH, 25 CPH, considering heave, surge, pitch motions and the connection line force. The spatial and temporal discretization are connected through the CFL condition. The maximum CLF number is set to 0.5, with the initial time step 0.01 s, which is afterwards modified automatically according to CLF condition.

Sea state 1, with the highest steepness, was selected for the evaluation of spatial discretization process and results are illustrated in Fig. 5. Afterwards, the results from the discretization study are analyzed using the relative discretization uncertainty,  $U$ . This is a metric quantity for the evaluation of different spatial discretization levels (Vukčević, 2016; Windt et al., 2019b) given by Eq. (6),

$$U = 100 \times \frac{U_a}{S_f} \quad (6)$$

where  $U_a$  is the absolute discretization uncertainty and  $S_f$  is the numerical solution from the case with the finest grid. As an initial step, it is necessary to define whether the discretization study converges. The discrimination ratio  $R_D$  provides information about the convergence or divergence of the study according to Table 5. Depending on

**Table 4**  
Boundary conditions for the NWT.

Variables	Inlet/Outlet	Seabed	Atmosphere	Side walls
alpha.water	waveAlpha <sup>a</sup> /zeroGradient	zeroGradient	inletOutlet	zeroGradient
Velocity	waveVelocity <sup>a</sup>	slip	pressureInletOutletVelocity	slip
Pressure	fixedFluxPressure	zeroGradient	totalPressure	fixedFluxPressure
$k$	zeroGradient	kqRWallFunction	inletOutlet	slip
$\omega$	zeroGradient	omegaWallFunction	inletOutlet	slip

<sup>a</sup>IHFOAM

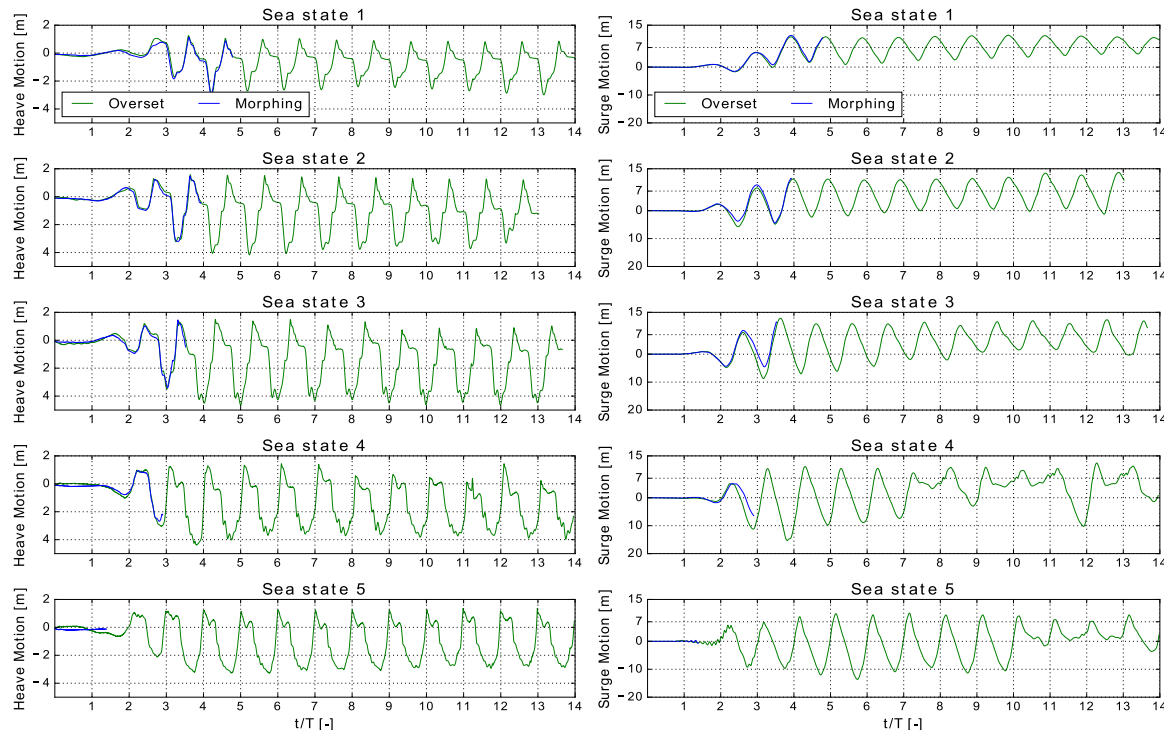


Fig. 6. Response in heave and surge motion, applying both DMMs for damping coefficient 59 kN.

**Table 5**  
Convergence based on discrimination ratio,  $R_D$ , criterion.

Type	Convergence	Divergence
Monotonic	$0 < R_D < 1$	$R_D < 0$ and $ R_D  < 1$
Oscillatory	$R_D > 1$	$R_D < 0$ and $ R_D  > 1$

the convergence type,  $U_a$  is calculated for monotonic and oscillatory convergence using Eqs. (8) and (9), respectively,

$$R_D = \frac{S_f - S_m}{S_m - S_c}, \quad (7)$$

$$U_a = F_s \frac{|S_f - S_m|}{r^p - 1}, \quad (8)$$

$$U_a = 0.5F_s |\max(S_f, S_m, S_c) - \min(S_f, S_m, S_c)| \quad (9)$$

$$p = \frac{\ln [(S_f - S_m)/(S_m - S_c)]}{\ln r}. \quad (10)$$

Here,  $r$  is the refinement ratio which is set to 2 in many applications,  $F_s$  is safety factor set to 1.25–1.5.  $p$  is the order of accuracy calculated by Eq. (10), the theoretical value of  $p$  is 2.  $S_m$  and  $S_c$  are the numerical solutions from the cases with medium and coarse grid, respectively.

Each one of the three motions: heave, surge and pitch and the connection line force are expressed as the mean value of 14 wave cycles simulation. The discrimination ratio,  $R_D$ , proves monotonic convergence for all the examined parameters. For the  $U$  calculation, three resolutions are examined; coarse, medium and fine. In Table 6, the response and  $U$  values for 16 CPH, 20 CPH and 25 CPH are listed.

**Table 6**  
Relative discretization uncertainty,  $U$  [%].

Parameter	16 CPH	20 CPH	25 CPH	U [%]
Heave [m]	3.51	3.85	3.96	1.52
Surge [m]	12.61	11.86	11.53	2.72
Pitch [m]	67.22	63.26	62.28	0.64
Line force [kN]	47.65	48.33	48.71	1.22

Having as reference the highest resolution case, the discretization uncertainty level shows satisfactory level of convergence,  $U < 3\%$ . Trying to balance between the computational cost and grid resolution accuracy, 20 CPH is considered for the rest of the present work for all the sea states.

### 3. Results and discussion

#### 3.1. Extreme wave–structure interaction modeling in OpenFOAM

One of the objectives of the present work is to simulate the extreme wave–structure interaction utilizing the overset method, implemented recently in OpenFOAM. The overset solution is compared with the commonly used morphing mesh method and the results are presented here.

For the damping coefficient equal to 59 kN, the WEC's response is illustrated in Figs. 6 and 7, with the blue and green lines expressing the morphing and overset DMMs, respectively. In general, the morphing

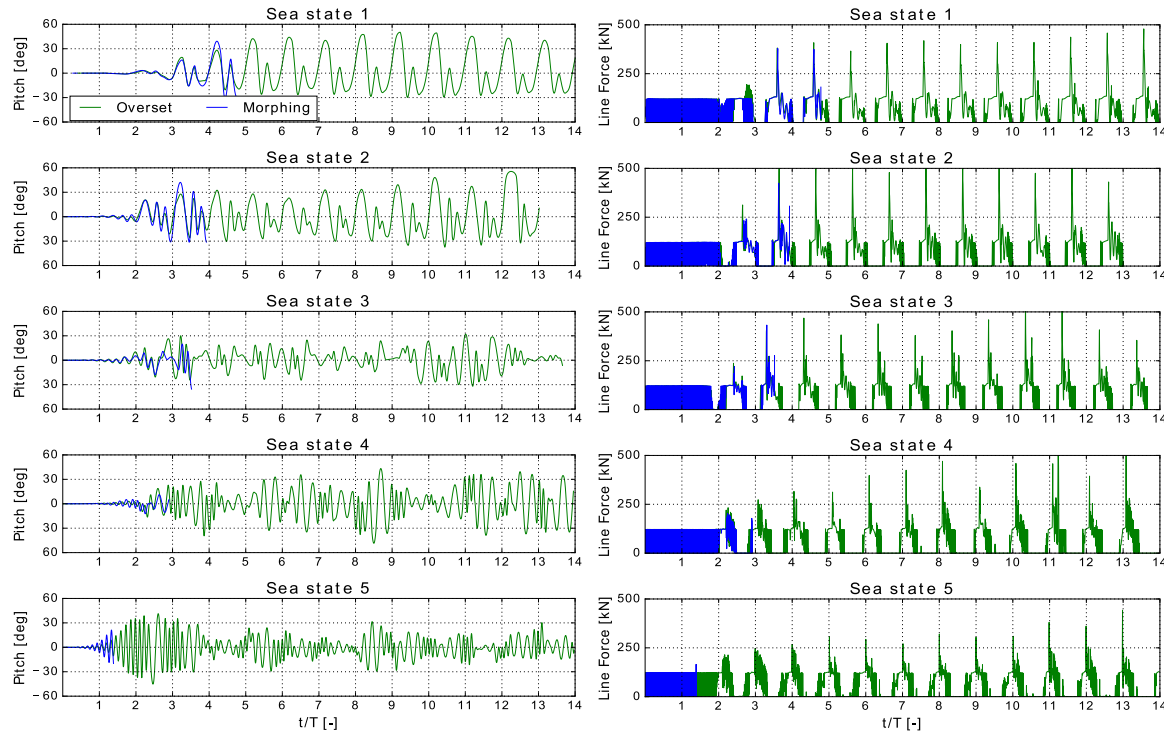


**Fig. 7.** Response in pitch motion and connection line force, applying both DMMs for damping coefficient 59 kN.

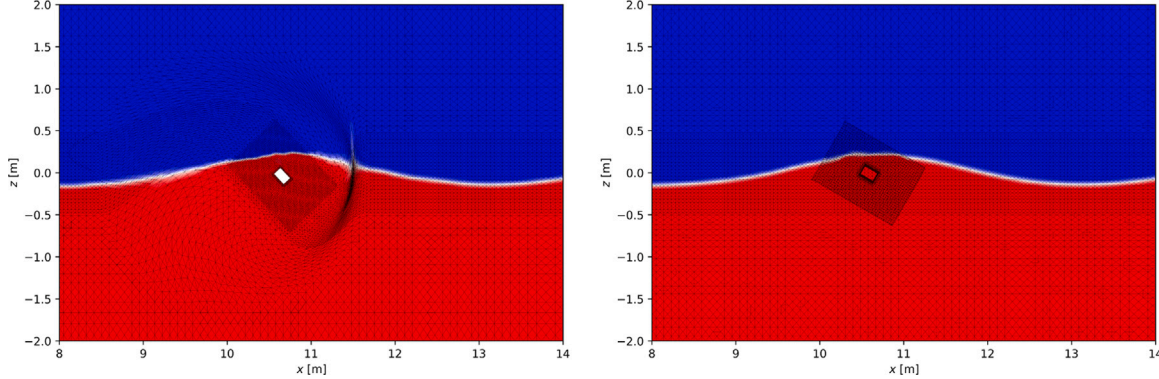


**Fig. 8.** Sea state 1: The computational mesh for morphing and overset DMMs is shown on the left and right picture, respectively.

mesh method fails to provide the solution for all of the examined sea states, yet the overset mesh leads to the successful completion showing that the method is able to handle large amplitude, multi-degree of freedom (DoF) WEC motion. At the same time instant the overset mesh method retains its mesh quality while the morphing mesh appears notable mesh deformation with high skewness cells, as it is shown in Fig. 8. At this point, it is interesting to study how the failure is related with the wave conditions and the system's behavior. At sea states 1, 2 and 3 the morphing mesh fails a few seconds after the heave motion has reached the maximum displacement for second time while the upper end-stop spring in the generator hull is compressed inducing snap load in the connection line. At the same time, the WEC has been displaced in the surge direction further from its initial position having great pitch response, and this is a combination leading the cells in the morphing zone area to stretch significantly degrading the mesh quality (Fig. 9, sea states 1 and 3). For sea states 4 and 5 the failure comes even earlier since the waves cause greater surge and pitch motion (Fig. 9, sea states 4 and 5), thus the computational mesh is deformed radically even from the first wave load cycles.

The `checkMesh` utility of OpenFOAM provides further information about the mesh quality, and it was found that more than 10000 face-cells, for each sea state, are severely non-orthogonal causing numerical instabilities. In general, the morphing mesh highly depends on the layout of the NWT and the proper choice of the `innerDistance` and `outerDistance`, which should be defined based on the amplitude of the buoy's motion. A priori knowledge of the WEC's dynamics is an advantage in order to implement the proper settings, but this is not usually feasible. In fact, the correct implementation of the morphing mesh demands preliminary study leading to an iterative simulation process until simulation stability is achieved, but this process demands time and resources.

For a quantitative assessment of the two methods the root-mean-square error (RMSE) is considered. The comparison evaluates the scenario with lower damping coefficient (59 kN). The methods agree well in terms of heave displacement, with the RMSE being approximately equal to 0.9%. However, this is not the case for the surge motion, the RMSE is slightly less than 4% for the sea states 1 and 2, but the RMSE increases with the increase of the wave height (sea states 3 and 4), and then drops again for the sea state 5 in which the wave height is

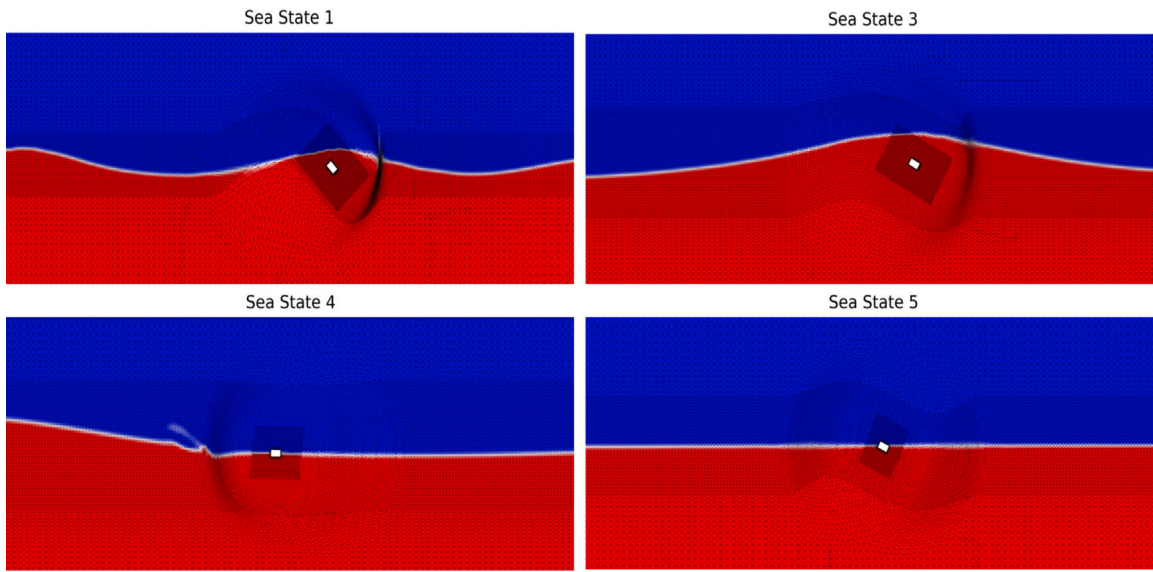


**Fig. 9.** Simulation of the wave–structure interaction utilizing the morphing DMM. The pictures show the mesh deformation at the time instant of simulation fatality.

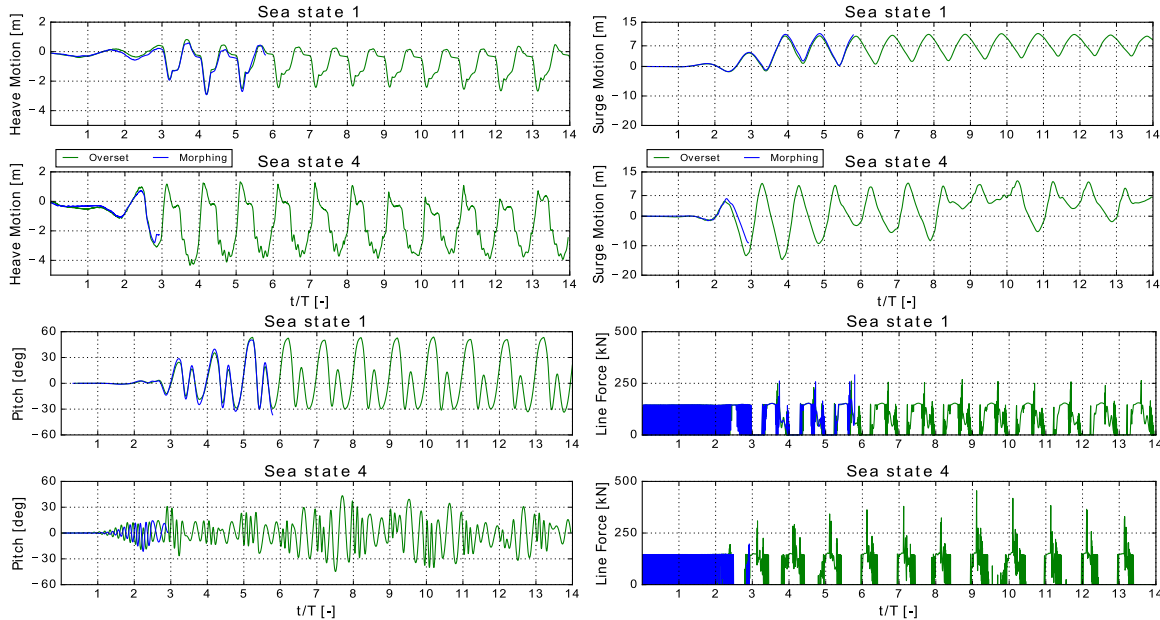


**Fig. 10.** Response in 3 DoF motion and connection line force, applying both DMMs for damping coefficient 83 kN.

**Table 7**

DMMs comparison through RMSE values, index 1 refers to the cases with damping coefficient= 59 kN, index 2 to damping coefficient 83 kN.

#	RMSE <sub>1</sub> [%]			RMSE <sub>2</sub> [%]		
	Heave	Surge	Pitch	Heave	Surge	Pitch
1	0.89	2.2	7.7	0.85	2.6	4.3
2	0.90	4.4	10	—	—	—
3	0.91	8	15	—	—	—
4	0.84	10.2	9	0.88	9.2	21
5	0.98	2	8.2	—	—	—

lower. In terms of the pitch motion the solution obtained from the two methods differs significantly; the RMSE value is higher than 7%, and the deviation is influenced for steep and high waves. The peak force is mainly dominated by the WEC's heave displacement, therefore, the two DMMs provide good agreement in the solutions.

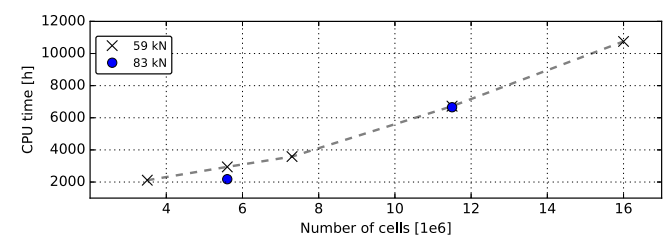


**Fig. 11.** CPU time for the solution of the overset mesh cases.

Now a higher damping coefficient is implemented, which is equal to 83 kN, and the WEC's response is evaluated in sea states 1 and 4. The reason of this choice relies on the fact that the wave is the steepest at sea state 1 while the wave has the maximum height at sea state 4. Figs. 10 shows that the higher damping does not necessarily help the

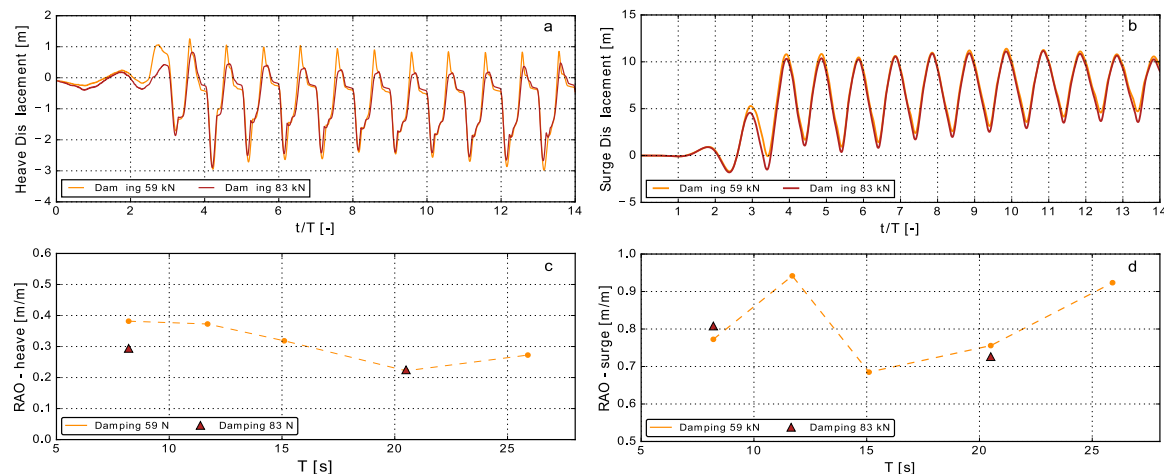


**Fig. 12.** The subfigure (a) express the time series of the buoy heave motion and (b) the buoy surge motion, during sea state 1, for two different dampings. The subfigures (c) and (d) depict the heave and surge RAOs, for all the examined sea states and dampings.

morphing mesh to complete the simulations; even though the heave displacement is reduced the surge and pitch motions are not much affected. For increased damping, the morphing mesh simulation runs for one more wave cycle during sea state 1, but the sea state 4 case fails again almost at the same time instant. The solutions are evaluated through the RMSE value, which appears the same behavior for the heave, surge and pitch DoF as previously, for damping coefficient 59 kN. In Table 7, all the RMSE values are listed.

### 3.1.1. CPU time

All the cases run on the Tetralith HPC cluster using 128 processors. In Fig. 11, the CPU hours required for the overset method are presented. Each simulation runs for 14 wave cycles ( $14T$ ) and the CPU time increases for sea states with longer waves (moving in the clock-wise direction along the contour). This is justified by the fact that the dimensions of the NWT are adapted to the wave length, as it is described in Section 2.4.1. The comparison with the morphing mesh is not included in this study because it fails to complete the full simulation.

### 3.2. WEC's response in extreme waves

This work is also dedicated to provide useful outcomes related to the WEC's response in 100-year return period waves. The control strategy of alternating damping coefficient is commonly applied during harsh environmental conditions and it can be alternated via electrical load control (Wang et al., 2020). Here, two damping coefficients are evaluated for the steepest wave (sea state 1) and highest wave (sea state 4) and the results are summarized in Table 8.

In general, the maximum heave displacement plays an important role because it is directly related to the loads on critical mechanical components; the upper end-stop spring and connection line. Fig. 12(a) compares the heave time series for damping coefficient 59 and 83 kN, during sea state 1. Fig. 12(c) shows the heave-RAOs for the examined sea states and damping coefficients. The heave-RAO is higher in waves with shorter period (steeper waves), while the increase in damping by 40% results in heave-RAO's reduction by 23% for the sea state 1 ( $T = 8.2$  s). At sea state 4 ( $T = 20.5$  s), the heave-RAO is not affected by the damping increase because the wave is already very high.

Fig. 12(b) shows that the surge motion does not change significantly when the damping is increased and this can justify the fact that the surge-RAO is almost unaffected for higher damping (Fig. 12(d)). The surge-RAO is maximized for the sea states 2 and 5, in which the wave height has a mid value (Fig. 12(d)).

**Table 8**

Percentage change [%] of WEC response for 40% increase in damping coefficient.

Parameter	Sea state 1	Sea state 4
RAO-heave	-61.8	+3
RAO-surge	-50	-7.4
Connection line force	-39	-12
Upper end-stop spring	-52.4	-18
Surge force	-27.7	-31

The force acting on the connection line is highly driven by the buoy's heave motion, Fig. 13(a) illustrates the force time series during sea states 1 and 4, when damping is equal to 59 kN. According to Fig. 13(c), the maximum snap load in the connection line is recorded during sea state 2 ( $T = 11.7$  s) and is equal to 500 kN. Although the sea state 4 ( $T = 20.5$  s) is characterized as the 100-year wave, the force in the connection line force is not the maximum, as someone would expect. The combination of wave steepness and wave height is what leads the sea state 2 to be the most critical for the connection line.

The upper end-stop spring is also a critical mechanical component with significant severity of failure because in such scenario the WEC has to be lifted, opened and repaired onshore. Fig. 13(b) and (d) show the compressed spring length divided by the total spring length. From Fig. 13(d), it can be concluded that the spring is compressed further during sea state 2 ( $T = 11.7$  s), yet the compression is reduced for increasing wave period (i.e. smaller steepness). It is worth noticing that for the examined sea states of the present study, the upper end-stop spring is never fully compressed. There is just an instantaneous full compression at  $t/T = 11$  during sea state 4.

The connection line, upper end-stop spring displacement and surge force are presented through colormap approach in Fig. 14, making it easier for the reader to evaluate the response in conjunction with 100-years return period sea states.

### 4. Conclusions

A point-absorber WEC connected to a direct-driven linear generator with limited stroke length has been examined for five extreme sea states along the 100-year environmental contour for the Humboldt Bay site, in California.

The first part of the present work focuses on the evaluation of OpenFOAM to handle large amplitude and multi-DoF response of the WEC interacting with extreme waves. The overset DMM was utilized and compared with the most commonly used DMM, which is the morphing mesh. The results show that overset mesh method provides stability

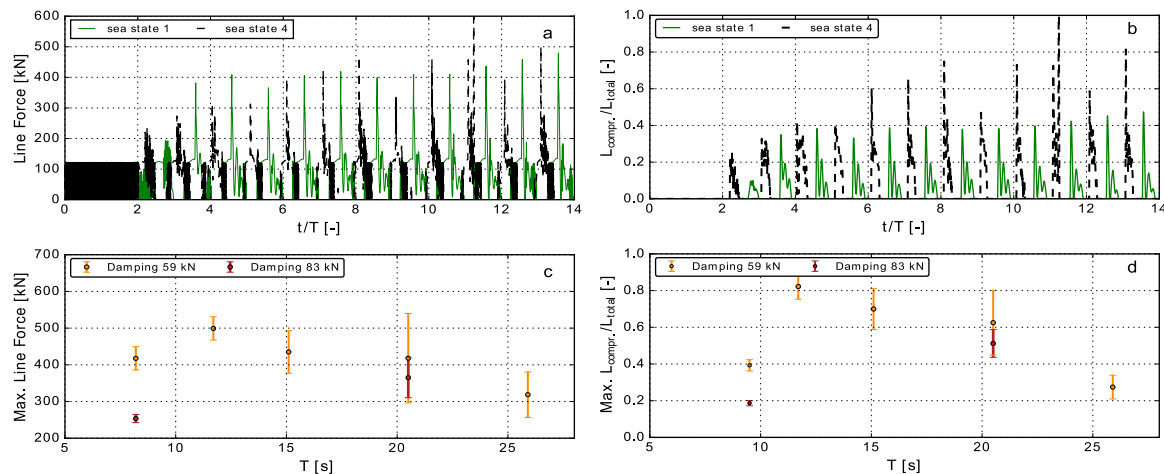


**Fig. 13.** The subfigure (a) express the time series of the force acting on the connection line and (b) the spring compression–spring length-ratio ( $L_{\text{compres.}}/L_{\text{total}}$ ), during sea state 1 and 4, for damping = 59 kN. The subfigures (c) and (d) depict the averaged maximum values and deviation of the previously mentioned quantities, for all the examined sea states and dampings.

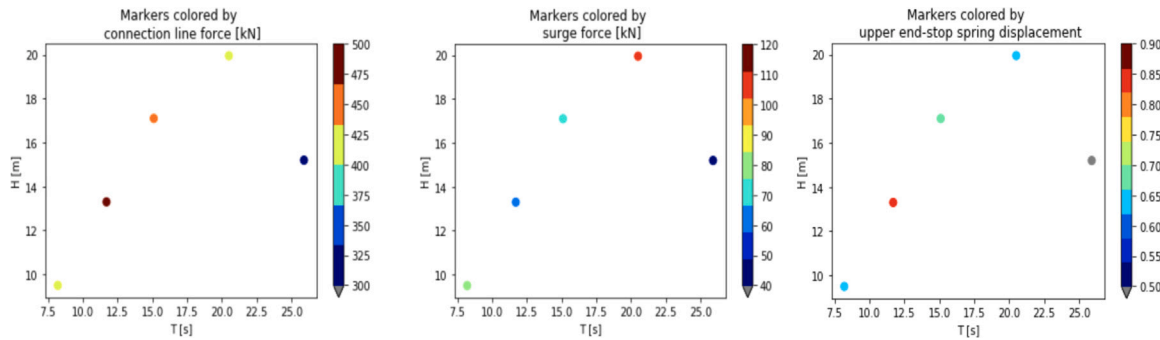


**Fig. 14.** Colormap depiction of WEC response in 100-year return period sea states.

and successfully completes the simulations for all the sea states. On the other hand, the morphing mesh fails due to numerical instability. The failure of morphing mesh simulation is mainly affected by the great surge and pitch motions of the buoy, inducing the deformation of the mesh quality. However, before the fatality of morphing mesh simulations, the solutions from the two DMMs are compared proving that there is good convergence in heave response and connection line force. The solution for surge and pitch response diverges, probably due to the high mesh deformation. In the current work, the increase of damping coefficient does not help the morphing mesh solution. Even though the higher damping reduces the heave-RAO, the surge and pitch motions are not much affected, which are the main reasons for the mesh quality degradation.

The second part of this work evaluates the WEC's response in 100-year waves. The wave characteristics, e.g. wave steepness and wave length, play important role in wave–structure interaction and their combination is critical. That is to say, the large wave height is definitely an important parameter, but smaller and steeper waves also should be evaluated. It has been concluded that the heave-RAO is higher for steeper waves, but the surge-RAO is larger for longer waves. The connection line and upper end-stop spring are two critical components of the system and the force acting on them is highly driven by the heave motion. For both components, the maximum value is recorded during sea state 2, which is not the case with the highest wave but the combination of high wave and steepness. The increase in damping coefficient by 40% reduces the snap loads on critical wave components and also reduces fluctuation of the load, therefore, it can be considered as a good practice during harsh environmental conditions.

As future work, it would be interesting to analyze the WEC dynamics by representing the extreme waves as focused waves or embedded

waves in a regular wave background. Moreover, the comparison with experimental results is also highly recommended.

#### CRediT authorship contribution statement

**Eirini Katsidoniaki:** Conceptualization, Methodology, Software, Formal analysis, Writing – original draft, Writing – review & editing. **Malin Göteman:** Conceptualization, Supervision, Project administration, Funding acquisition, Writing – review & editing.

#### Declaration of competing interest

The authors declare that they have no known competing financial interests or personal relationships that could have appeared to influence the work reported in this paper.

#### Acknowledgments

The authors wish to thank Dr. Yi-Hsiang Yu, NREL of the USA, for useful comments on the manuscript.

The research in this paper was supported by the Centre of Natural Hazards and Disaster Science, Sweden, the Swedish Research Council (VR, grant number 2015-04657), the Swedish Energy Authority (project number 47264-1). This scientific paper was also supported by the Onassis Foundation, scholarship ID: F ZP 021-1/2019-2020.

The CFD simulations were performed on resources provided by the Swedish National Infrastructure for Computing (SNIC) at the HPC cluster: Tetralith at the National Supercomputer Centre, Linköping University.

## References

- Chaplin, J., Rainey, R., 2012. Long duration experiments in irregular waves, to determine 10,000-year wave loads on a 3.5 m diameter vertical cylinder.
- Chen, W., Dolguntseva, I., Savin, A., Zhang, Y., Li, W., Svensson, O., Leijon, M., 2017. Numerical modelling of a point-absorbing wave energy converter in irregular and extreme waves. *Appl. Ocean Res.* 63, 90–105.
- Chen, H., Qian, L., Ma, Z., Bai, W., Li, Y., Causon, D., Mingham, C., 2019a. Application of an overset mesh based numerical wave tank for modelling realistic free-surface hydrodynamic problems. *Ocean Eng.* 176, 97–117.
- Chen, H., Qian, L., Ma, Z., Bai, W., Lin, Z., et al., 2019b. CCP-WSI blind test series 3: OpenFOAM simulation of focused wave interaction with a simplified wave energy converter. In: The 29th International Ocean and Polar Engineering Conference. International Society of Offshore and Polar Engineers.
- Coe, R.G., Neary, V.S., Lawson, M., Yu, Y., Weber, J., 2014. Extreme Conditions Modeling Workshop Report. Technical Report, National Renewable Energy Lab.(NREL), Golden, CO (United States).
- Coe, R.G., Yu, Y.-H., Van Rij, J., 2018. A survey of WEC reliability, survival and design practices. *Energies* 11 (1), 4.
- Davidson, L., 2015. An introduction to turbulence models. Citeseer.
- Davidson, J., Karimov, M., Szelechman, A., Windt, C., Ringwood, J., 2019. Dynamic mesh motion in OpenFOAM for wave energy converter simulation. In: 14th OpenFOAM Workshop.
- DNV, 2010. Environmental Conditions and Environmental Loads, Recommended Practice. Technical Report, Det Norske Veritas.
- Engström, J., Sjökvist, L., Göteman, M., Eriksson, M., Hann, M., Ransley, E., Greaves, D., Leijon, M., 2017. Buoy geometry and its influence on survivability for a point absorbing wave energy converter: Scale experiment and CFD simulations, Washington, DC, USA.
- European Commission, 2020. An EU strategy to harness the potential of offshore renewable energy for a climate neutral future. Technical Report, (SWD (2020) 273 final), European Commission.
- Folley, M., 2016. Numerical Modelling of Wave Energy Converters: State-of-the-Art Techniques for Single Devices and Arrays. Academic Press.
- Giorgi, G., Ringwood, J.V., 2017. Computationally efficient nonlinear Froude–Krylov force calculations for heaving axisymmetric wave energy point absorbers. *J. Ocean Eng. Mar. Energy* 3 (1), 21–33.
- Göteman, M., Engström, J., Eriksson, M., Hann, M., Ransley, E., Greaves, D., Leijon, M., 2015. Wave loads on a point-absorbing wave energy device in extreme waves. *J. Ocean Wind Energy* 2 (3), 176–181.
- Guerrero, J., 2006. Overset Composite Grids for the Simulation of Complex Moving Geometries. DICAT, University of Genoa, Italy.
- Higuera, P., Lara, J.L., Losada, I.J., 2013. Realistic wave generation and active wave absorption for Navier–Stokes models: Application to OpenFOAM®. *Coast. Eng.* 71, 102–118.
- International Electrotechnical Commission, 2015. Marine energy: wave, tidal and other water current converters. tidal energy resource assessment and characterization.
- International Electrotechnical Commission, 2019. IEC TS 62600-2:2019, Technical Report 2019. Available online:Technical Report.
- Jasak, H., Tuković, Ž., 2010. Dynamic mesh handling in OpenFOAM applied to fluid-structure interaction simulations. In: Proceedings of the V European Conference on Computational Fluid Dynamics ECCOMAS CFD 2010.
- Jenne, D.S., Yu, Y.-H., Neary, V., 2015. Levelized cost of energy analysis of marine and hydrokinetic reference models. Technical Report, National Renewable Energy Lab.(NREL), Golden, CO (United States).
- Katsidoniaki, E., Göteman, M., 2020. Comparison of dynamic mesh methods in openfoam for a WEC in extreme waves. In: Developments in Renewable Energies Offshore. CRC Press, pp. 214–222.
- Katsidoniaki, E., Nilsson, E., Rutgersson, A., Engström, J., Göteman, M., 2021. Response of point-absorbing wave energy conversion system in 50-years return period extreme focused waves. *J. Mar. Sci. Eng.* 9 (3), 345.
- Katsidoniaki, E., Ransley, E., Brown, S., Palm, J., Engström, J., Göteman, M., 2020. Loads on a point-absorber wave energy converter in regular and focused extreme wave events. In: ASME 2020 39th International Conference on Ocean, Offshore and Arctic Engineering. American Society of Mechanical Engineers Digital Collection.
- Keulegan, G.H., Carpenter, L.H., 1958. Forces on cylinders and plates in an oscillating fluid. *J. Res. Natl. Bur. Stand.* 60 (5), 423–440.
- Kim, J.W., Jang, H., Baquet, A., O'Sullivan, J., Lee, S., Kim, B., Jasak, H., 2016. Technical and economic readiness review of CFD-Based numerical wave basin for offshore floater design. In: Proceedings of the Offshore Technology Conference.
- Leijon, M., Waters, R., Rahm, M., Svensson, O., Boström, C., Strömstedt, E., Engström, J., Tyrberg, S., Savin, A., Gravrakmo, H., et al., 2008. Catch the wave to electricity. *IEEE Power Energy Mag.* 7 (1), 50–54.
- Lemaire, S., Vaz, G., Turnock, S., 2019. On the need for higher order interpolation with overset grid methods.
- Magagna, D., Monfardini, R., Uihlein, A., 2016. JRC Ocean Energy Status Report 2016 Edition. Publications Office of the European Union, Luxembourg.
- Miquel, A.M., Kamath, A., Alagan Chella, M., Archetti, R., Bihs, H., 2018. Analysis of different methods for wave generation and absorption in a CFD-based numerical wave tank. *J. Mar. Sci. Eng.* 6 (2), 73.
- Neary, V.S., Lawson, M., Previsic, M., Copping, A., Hallett, K.C., LaBonte, A., Rieks, J., Murray, D., 2014. Methodology for Design and Economic Analysis of Marine Energy Conversion (MEC) Technologies. Technical Report, Sandia National Lab.(SNL-NM), Albuquerque, NM (United States).
- Norsk Standard, 2007. Actions and Action Effects. Technical Report N-003, Oslo: Norwegian Technology Standards Institution.
- Ochi, M.K., 2005. Ocean Waves: The Stochastic Approach, Vol. 6. Cambridge University Press.
- Ong, M.C., 2017. CFD applications in offshore engineering. In: EPJ Web of Conferences, Vol. 143. EDP Sciences, p. 01002.
- Palm, J., Eskilsson, C., Paredes, G.M., Bergdahl, L., 2016. Coupled mooring analysis for floating wave energy converters using CFD: Formulation and validation. *Int. J. Mar. Energy* 16, 83–99.
- Quon, E., Platt, A., Yu, Y.-H., Lawson, M., 2016. Application of the most likely extreme response method for wave energy converters. In: ASME 2016 35th International Conference on Ocean, Offshore and Arctic Engineering. American Society of Mechanical Engineers Digital Collection.
- Ransley, E., Greaves, D., Raby, A., Simmonds, D., Hann, M., 2017a. Survivability of wave energy converters using CFD. *Renew. Energy* 109, 235–247.
- Ransley, E., Greaves, D., Raby, A., Simmonds, D., Jakobsen, M.M., Kramer, M., 2017b. RANS-VOF modelling of the wavestar point absorber. *Renew. Energy* 109, 49–65.
- Roache, P.J., 1998. Verification and Validation in Computational Science and Engineering, Vol. 895. Hermosa Albuquerque, NM.
- Shoemake, K., 1985. Animating rotation with quaternion curves. In: Proceedings of the 12th Annual Conference on Computer Graphics and Interactive Techniques, pp. 245–254.
- Sjökvist, L., Göteman, M., 2016. The effect of overtopping waves on peak forces on a point absorbing WEC. In: Proceedings of the Asian Wave and Tidal Energy Conference Series AWTEC, Singapore, pp. 24–28.
- Sjökvist, L., Göteman, M., 2019. Peak forces on a point absorbing wave energy converter impacted by tsunami waves. *Renew. Energy* 133, 1024–1033.
- Sjökvist, L., Wu, J., Ransley, E., Engström, J., Eriksson, M., Göteman, M., 2017. Numerical models for the motion and forces of point-absorbing wave energy converters in extreme waves. *Ocean Eng.* 145, 1–14.
- Van Rij, J., Yu, Y.-H., Coe, R.G., 2018. Design load analysis for wave energy converters. In: ASME 2018 37th International Conference on Ocean, Offshore and Arctic Engineering. American Society of Mechanical Engineers Digital Collection.
- Vukčević, V., 2016. Numerical modelling of coupled potential and viscous flow for marine applications (Ph.D. thesis). Fakultet strojarstva i brodogradnje, Sveučilište u Zagrebu.
- Wang, L., Lin, M., Tedeschi, E., Engström, J., Isberg, J., 2020. Improving electric power generation of a standalone wave energy converter via optimal electric load control. *Energy* 211, 118945.
- Weller, H., McIntyre, W.A., 2019. Numerical solution of the conditionally averaged equations for representing net mass flux due to convection. *Q. J. R. Meteorol. Soc.* 145 (721), 1337–1353.
- Windt, C., Davidson, J., Akram, B., Ringwood, J.V., 2018a. Performance assessment of the overset grid method for numerical wave tank experiments in the openfoam environment. In: International Conference on Offshore Mechanics and Arctic Engineering, Vol. 51319. American Society of Mechanical Engineers, V010T09A006.
- Windt, C., Davidson, J., Chandar, D.D., Faedo, N., Ringwood, J.V., 2020a. Evaluation of the overset grid method for control studies of wave energy converters in OpenFOAM numerical wave tanks. *J. Ocean Eng. Mar. Energy* 6 (1), 55–70.
- Windt, C., Davidson, J., Chandar, D., Ringwood, J.V., 2019a. On the importance of advanced mesh motion methods for WEC experiments in CFD-based numerical wave tanks. In: MARINE VIII: Proceedings of the VIII International Conference on Computational Methods in Marine Engineering. CIMNE, pp. 145–156.
- Windt, C., Davidson, J., Ransley, E.J., Greaves, D., Jakobsen, M., Kramer, M., Ringwood, J.V., 2020b. Validation of a CFD-based numerical wave tank model for the power production assessment of the wavestar ocean wave energy converter. *Renew. Energy* 146, 2499–2516.
- Windt, C., Davidson, J., Ringwood, J.V., 2018b. High-fidelity numerical modelling of ocean wave energy systems: A review of computational fluid dynamics-based numerical wave tanks. *Renew. Sustain. Energy Rev.* 93, 610–630.
- Windt, C., Davidson, J., Schmitt, P., Ringwood, J.V., 2019b. On the assessment of numerical wave makers in CFD simulations. *J. Mar. Sci. Eng.* 7 (2), 47.
- Wolgamot, H.A., Fitzgerald, C.J., 2015. Nonlinear hydrodynamic and real fluid effects on wave energy converters. *Proc. Inst. Mech. Eng. A J. Power Energy* 229 (7), 772–794.
- World Bank, 2017. The Potential of the Blue Economy: Increasing Long-Term Benefits of the Sustainable Use of Marine Resources for Small Island Developing States and Coastal Least Developed Countries. Technical Report, United Nations Department of Economic and Social Affairs.
- Wrang, L., Katsidoniaki, E., Nilsson, E., Rutgersson, A., Rydén, J., Göteman, M., 2021. Comparative analysis of environmental contour approaches to estimating extreme waves for offshore installations for the baltic sea and the north sea. *J. Mar. Sci. Eng.* 9 (1), 96.
- Yu, Y.-H., Van Rij, J., Coe, R., Lawson, M., 2015. Preliminary wave energy converters extreme load analysis. In: ASME 2015 34th International Conference on Ocean, Offshore and Arctic Engineering. American Society of Mechanical Engineers Digital Collection.